Remote Sensing of Environment xxx (2011) xxx–xxx

Contents lists available at SciVerse ScienceDirect

Remote Sensing of Environment

journal homepage: www.elsevier.com/locate/rse

Improving the estimation of urban surface emissivity based on sub-pixel classification of high resolution satellite imagery

Zina Mitraka [a,c,*], Nektarios Chrysoulakis [a], Yiannis Kamarianakis [b], Panagiotis Partsinevelos [c], Androniki Tsouchlaraki [c]

[a] Foundation for Research and Technology, Hellas, Institute of Applied and Computational Mathematics, N. Plastira 100, Vassilika Vouton, P.O. Box 1385, GR-71110, Heraklion, Greece
[b] School of Civil and Environmental Engineering, Cornell University, USA
[c] Technical University of Crete, Greece

ARTICLE INFO

Available online xxxx

Keywords:
Land surface emissivity
Urban environment
Spectral mixture analysis
Constrained least absolute value algorithm

ABSTRACT

Information about the spatial distribution of urban surface emissivity is essential for surface temperature estimation. The latter is critical in many applications, such as estimation of surface sensible and latent heat fluxes, energy budget, urban canopy modeling, bio-climatic studies and urban planning. This study proposes a new method for improving the estimation of urban surface emissivity, which is primarily based on spectral mixture analysis. The urban surface is assumed to consist of three fundamental land cover components, namely vegetation, impervious and soil that refer to the urban environment. Due to the complexity of the urban environment, the impervious component is further divided into two land cover components: high-albedo and low-albedo impervious. Emissivity values are assigned to each component based on emissivity distributions derived from the ASTER Spectral Library Version 2.0. The fractional covers are estimated using a constrained least absolute values algorithm which is robust to outliers, and results are compared against the ones derived from a conventional constrained least squares algorithm. Following the proposed method, by combining the fraction of each cover component with a respective emissivity value, an overall emissivity for a given pixel is estimated. The methodology is applicable to visible and near infrared satellite imagery, therefore it could be used to derive emissivity maps from most multispectral satellite sensors. The proposed approach was applied to ASTER multispectral data for the city of Heraklion, Greece. Emissivity, as well as land surface temperature maps in the spectral region of 10.25–10.95 μm (ASTER band 13) were derived and evaluated against ASTER higher level products revealing comparable error estimations. An overall RMSE of 0.014776 (bias = −0.01239) was computed between the estimated emissivity obtained using the proposed methodology and the ASTER higher level product emissivity (AST05). The respective overall RMSE value for derived LST was found equal to 0.816935 K (bias = 0.67826 K).

1. Introduction

While cities cover only a small portion of the global land surface, most of the human population and related activities are concentrated in the urban environment, resulting in significant transformation of natural resources (Kennedy et al., 2011; Lambin et al., 2001). During the last decade, there has been a growing interest in studies concerning surface temperatures and urban energy budget characteristics. Such knowledge is significant to a range of topics in earth sciences, including urban climatology (Arnfield, 2003; Voogt & Oke, 2003), global environmental change, human–environment interactions, (Weng, 2009; Yang et al., 2003) and planning and management practices (Chrysoulakis et al., 2009). The energy budget of the urban surface is mainly defined by its albedo and Land Surface Temperature (LST), both of which can be derived from satellite observations (Chrysoulakis, 2003). To retrieve LST from satellite observations, three main effects have to be considered and corrected: angular, emissivity and atmospheric effects. Jiménez-Muñoz and Sobrino (2003) analyzed these effects and found that 1% uncertainty in emissivity can lead to an error on the LST up to 0.4 K.

Emissivity is a measure of the inherent efficiency of the surface to convert heat energy into radiant energy. Satellite-based emissivity estimates depend largely on the composition, roughness and other physical parameters of the surface, such as its moisture content (Becker & Li, 1990, 1995). By definition, the channel emissivity ε_i is given by Becker and Li (1990):

$$\varepsilon_i = \frac{\int f_i(\lambda)\varepsilon_\lambda B_\lambda(LST)d\lambda}{\int f_i(\lambda)B_\lambda(LST)d\lambda} \quad (1)$$

* Corresponding author at: Foundation for Research and Technology, Hellas, Institute of Applied and Computational Mathematics, N. Plastira 100, Vassilika Vouton, P.O. Box 1385, GR-71110, Heraklion, Greece. Tel.: +30 2810 391771, +30 6944240944 (Mobile); fax: +30 2810391761.
E-mail address: mitraka@iacm.forth.gr (Z. Mitraka).

0034-4257/$ – see front matter © 2011 Elsevier Inc. All rights reserved.
doi:10.1016/j.rse.2011.06.025

where $B_\lambda(LST)$ is the Planck's function for black body emission, $f_i(\lambda)$ is the spectral response of the radiometer in channel i and ε_λ is the spectral emissivity. Although in Eq. (1), ε_i depends on LST, according to Becker and Li (1990), this variation of ε_i with LST is negligible ($\Delta\varepsilon_i = 10^{-4}$). Therefore, the channel emissivity can be expressed as:

$$\varepsilon_i = \frac{\int f_i(\lambda)\varepsilon_\lambda d\lambda}{\int f_i(\lambda) d\lambda} \quad (2)$$

The emissivity dependence on the physical condition of the surface imposes large temporal variations. This leads to a more complex undertaking of LST retrieval, often prone to largely varying and inconsistent accuracies. The emissivity of the surface affects the radiance measured from satellite sensors primarily in three significant ways (Prata, 1993): a) the reduction of emissivity from unity causes a reduction in the magnitude of the upwelling surface radiance; b) the nonblack behavior of the surface gives rise to a contribution from the reflected radiance from the surface; c) the anisotropy of the reflectivity and emissivity of the surface can substantially modify the total radiance received at the satellite. Other factors associated with surface emissivity effects are mixed pixel effects and zenith angle effects.

The main problem in determining emissivity from Eq. (2) is the observation of emissivity of natural surfaces at satellite spectral and spatial resolutions (Coll et al., 1994). The dimension of ground pixels in a satellite image is such that the characteristics of the surface may display substantial variation within a pixel. For instance, surface temperatures can vary by as much as 10 K over a few meters due to shadowing effects, variation in insolation and topographic effects (Prata, 1993). This strong horizontal heterogeneity introduces ambiguity to the definition of an overall emissivity and LST for a given pixel at a given scale. Furthermore ambiguity rises from emissivity, LST and their correlation measured at different scales, for instance, from different satellite sensors, or in-situ derived. This scale mismatch also makes validation against “ground truth” difficult.

By changing the viewing angle of the radiometer, the radiation mix from the same components is affected (Prata, 1994). Most natural surfaces show angular variation of emissivity higher or equal to 0.01, for viewing angles higher than 30° (Sobrino & Cuenca, 1999). These differences lead to absolute errors on LST equal to or higher than 0.4 K. As discussed by Sobrino et al. (1996), estimation of the angular variation of emissivity is a difficult problem, since there are only very few in-situ measurements of the angular variation of emissivity over land. Prata (1994) proposed a parameterization for the angular variation of emissivity for bare soil. For dry, bare surfaces, emissivity effects on LST are more important and need to be specified within an accuracy of ± 0.005. For vegetated surfaces, emissivity effects are minimized by cavity effects and angular effects are only important for structured vegetation (Sobrino et al., 1990). As explained by Prata (1994), cavity effects tend to increase the emissivity and reduce the spectral contrast.

Several methods have been developed to retrieve surface emissivity (Becker & Li, 1990; Kealy & Gabell, 1990; Snyder et al., 1998; Sobrino & Raissouni, 2000; Valor & Casseles, 1996; Watson, 1992). Dash et al. (2002) summarized different emissivity estimation techniques and analyzed their main constraints. Within a particular surface type, emissivity variation is not well known, but measurements suggest it is small, around ± 0.01, except when structural changes occur as in senescent vegetation. Thus, as explained by Prata (2002), the greatest concern for deriving LSTs is variation between (rather than within) surface types. The scheme for accounting for emissivity variations between surface types relies on a surrogate measure of surface structure. ASTER higher level emissivity and LST products are derived using the Temperature Emissivity Separation method (TES) (Gillespie et al., 1998). TES products have been validated and were found to perform within the specification of ± 0.015 for emissivity and ± 1.5 K for LST (Gillespie et al., 1998). Jiménez-Muñoz et al. (2006) developed an emissivity retrieval method for ASTER based on Normalized Vegetation Index (NDVI). Snyder et al. (1998) proposed a classification-based method to estimate emissivity from conventional static land cover classes and dynamic information, and developed an emissivity knowledge-base. Snyder et al. (1998) derived spectral coefficients from laboratory measurements of material samples (Salisbury et al., 1994; Salisbury & D'Aria, 1992, 1994; Snyder et al., 1997) with the use of linear Bidirectional Reflectance Distribution Function models and structural parameters from approximate descriptions of the cover type (Snyder & Wan, 1998). Uncertainties on estimated emissivity, when land-cover mapping methods are applied, are due to the limited number of land-cover types and the lack of updates in land-cover maps. LST errors increase almost linearly, and may reach 6 K in absolute magnitude for fairly small errors in emissivity (Yu et al., 2008).

Mapping the urban environment in terms of its physical components preserves the heterogeneity of urban land cover better than traditional land-use classification (Clapham, 2003; Ji & Jensen, 1999), characterizes urban land cover independent from analyst-imposed definitions (Jensen, 1983; Ridd, 1995), and captures accurately changes through time (Ji & Jensen, 1999; Rashed et al., 2005). The Vegetation-Impervious-Soil (VIS) model (Ridd, 1995) considers the combination of impervious surfaces, green vegetation, and exposed soil as the fundamental components of urban ecosystems if water surfaces are ignored. Lu and Weng (2004) refer to a number of studies where the VIS model is applied to characterize urban environments.

In this paper, a new methodology for estimating land surface emissivity from high resolution satellite imagery is proposed. The urban land cover is modeled using a variant of VIS model (Ridd, 1995) and the sub-pixel components of land cover are mapped using Spectral Mixture Analysis (SMA). Assuming that land surface emissivity can be expressed as a linear combination of the emissivities of all components inside a pixel, the spatial distribution of emissivity can be derived from visible and near infrared satellite observations.

2. Study area and datasets

The study area covers the broader area (approximately 360 km^2) of Heraklion, the larger city in the island of Crete, Greece (Fig. 1). Heraklion is one of the rapidly growing urban areas in Greece and exhibits a mixed land-use pattern that includes residential, commercial and industrial surfaces, transportation networks and rural surfaces. This area is suitable for analysis as it possesses a diversified urban and rural land cover.

An Advanced Spaceborne Thermal Emission and Reflection Radiometer (ASTER) image (Level 1B) acquired on July 10, 2006 (acquisition time approximately 09:10 UTC) under clear weather conditions, was used in this study (Fig.1). ASTER imagery contains four visible and near infrared (VNIR), five shortwave infrared (SWIR) and five thermal infrared (TIR) bands of spatial resolution 15 m × 15 m, 30 m × 30 m and 90 m × 90 m respectively. ASTER higher level products (for both land surface temperature and emissivity) were also available for the respective scene (LPDAAC, 2010). Therefore, the available surface emissivity and temperature maps were used to evaluate the performance of the proposed method and perform accuracy assessment.

A very high resolution orthophotomap derived from Ikonos satellite image acquired during the same period (Summer 2006) was also made available by Foundation for Research and Technology — Hellas (FORTH). This orthophotomap was used as an ancillary dataset for the selection of endmembers on ASTER multispectral imagery. Finally, MODIS derived precipitable water product was used to consider the atmospheric effects, while estimating LST as per Jiménez-Muñoz and Sobrino (2010).

Please cite this article as: Mitraka, Z., et al., Improving the estimation of urban surface emissivity based on sub-pixel classification of high resolution satellite imagery, *Remote Sensing of Environment* (2011), doi:10.1016/j.rse.2011.06.025

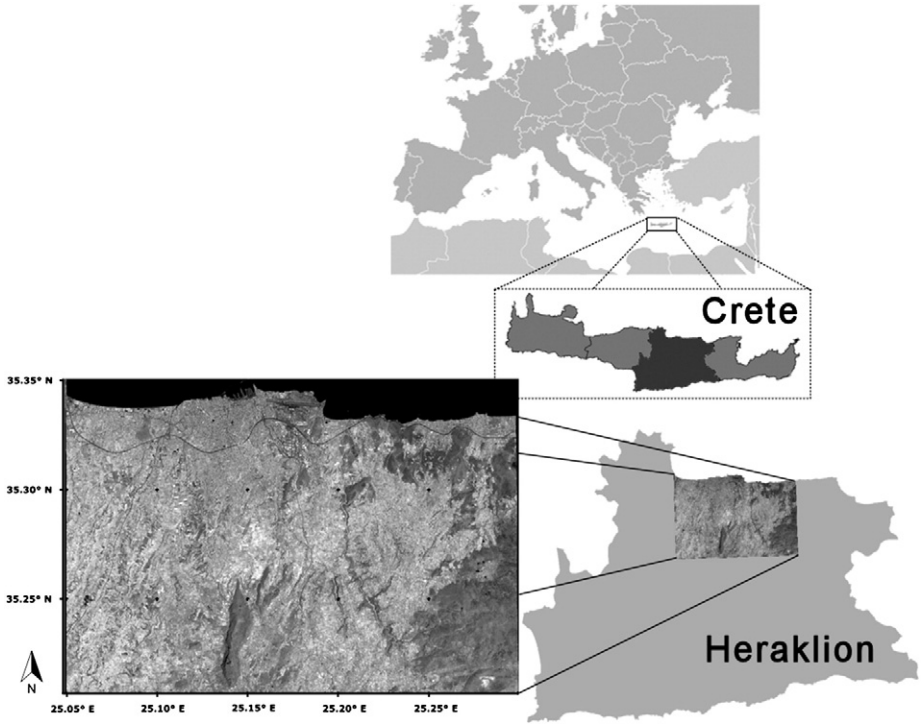

Fig. 1. The study area — the broader area of city of Heraklion in Crete Island, Greece.

3. Methodology

SMA was applied to compute the fraction of each land cover component in the scene. Emissivity density functions were created for these components based on the ASTER Spectral Library Version 2.0 (Baldridge et al., 2009). The derived fractions were combined with emissivity density functions to estimate the spatial distribution of surface emissivity. All steps followed to derive land surface emissivity based on SMA are explained below.

3.1. Image pre-processing

A pre-processing of the available images was necessary. The ASTER image was orthorectified to be combined with higher resolution data as in Chrysoulakis et al. (2010) and a 15 m posting was obtained. Digital numbers were converted to radiance values using recalibration coefficients generated by a modified version of Tonooka et al. (2003); SMA was performed using radiance values. The separate single bands of SWIR (5–9) were resampled (using nearest neighbor resampling) to pixel size of 15 m × 15 m to preserve the spatial resolution provided by the VNIR (1–4) bands. Nearest neighbor resampling is appropriate since all measurements are from the same sensor. It is considered essential to preserve as high a spatial resolution as possible, in order to eventually derive high spatial resolution emissivity maps. Up-scaling is possible since SMA is employed and information from lower spatial resolution bands can be exploited in spectral unmixing. Although atmospheric correction is essential when extracting land surface parameters from satellite images, in this case atmospheric correction was not necessary before SMA implementation, because the endmembers were collected using the same ASTER image. According to Song et al. (2001), in the case of image endmembers, atmospheric correction does not affect the results of SMA.

Heraklion is a coastal city, hence water is an important component of the scene. In this study, sea water is treated separately. Dark pixels are highly degenerate (i.e. they can be modeled successfully by a large shade fraction and a small bright fraction of almost any material), therefore they cannot be modeled accurately using SMA (Powell et al., 2007). A water mask, based on shoreline feature extraction (Lipakis et al., 2008), was applied to the image and pixels corresponding to sea water were removed from the analysis.

3.2. Linear spectral mixture analysis

Linear Spectral Mixture Analysis (LSMA) (Adams et al., 1995) was used to analyze the mixed pixels of the urban environment (Lu & Weng, 2006; Weng et al., 2006). The underlying urban landscapes are assumed to be composed of a few fundamental components, called endmembers. LSMA is a physically based image processing method that assumes the spectrum measured by a sensor to be a linear combination of the spectra of all components within the pixel. The spectral reflectance in band i can be described as:

$$R_i = \sum_{k=1}^{n} f_k R_{ik} + ER_i \tag{3}$$

where n is the number of endmembers, f_k is the fraction of endmember k within the pixel, R_{ik} is the known spectral reflectance of endmember k in band i and ER_i is the error for band i. The fractions of one pixel must sum to 1 and all fractions must be greater than or equal to zero. These conditions can be described by:

$$\sum_{k=1}^{n} f_k = 1$$
$$f_k \geq 0 \text{ for } k = 1, \ldots, n. \tag{4}$$

The fractional cover of each urban component is estimated using Eq. (3) constrained by the conditions of expression (4); hence, LSMA is a constrained linear regression problem. Similar to ordinary regression analysis where minimization of the sum of squared errors is the most common method for obtaining the unknown coefficients, coefficients of LSMA are estimated using a constrained least squares

Please cite this article as: Mitraka, Z., et al., Improving the estimation of urban surface emissivity based on sub-pixel classification of high resolution satellite imagery, *Remote Sensing of Environment* (2011), doi:10.1016/j.rse.2011.06.025

algorithm (see for instance Ramsey & Christensen, 1998). Minimization of the sum of least absolute values of errors is a natural alternative criterion to least squares which is more appropriate when the distribution of errors is skewed (Dielman, 2009). Furthermore, by minimizing sums of absolute values rather than sums of squares the effect of outliers in the coefficient estimates is diminished (Dielman, 2005). Therefore in this work, both constrained least squares (CLS) and constrained least absolute values (CLAV) algorithms were applied to derive the land cover fractions in (3). The algorithm described by Gill et al. (1981) was used for CLS, whereas for CLAV the algorithm provided in Koenker (2011) was used.

3.3. Endmembers selection

The selection of the endmembers is a critical step in LSMA, as development of high-quality fraction images depends greatly on the selection of suitable endmembers. In addition, when fraction images are used for physical parameters derivation such as emissivity, the correspondence between endmembers and reference emissivity values should also be taken into account. A variety of methods are used to determine endmembers either from spectral libraries or from field reflectance measurements (Powell et al., 2007), from the image itself (Boardman et al, 1995; Weng et al., 2009), or even from the combination of image and reference endmembers (Roberts et al., 1993; Smith et al., 1990).

In this study, land cover was modeled using a variation of the VIS model proposed in Ridd (1995). The urban environment was assumed to be composed of three fundamental components named vegetation, impervious and soil. The first component mainly refers to green vegetation. The impervious component in urban environment refers to manmade surfaces which vary widely in spectral response. Two main categories of impervious surface components were assumed: a high-albedo and a low-albedo component (Lu & Weng, 2006). Bright impervious surface information is included in the high-albedo component while dark impervious surface information is included in the low-albedo component.

Following the LSMA approach, each urban land cover component is assigned an endmember, which represents the respective component. Endmembers can be described as extremes in the spectral multidimensional space of the image (Weng et al., 2006). The Pixel Purity Index (PPI) (Boardman et al., 1995) was used as a first step to identify spectrally pure pixels. PPI was not applied directly to the image, but to its Minimum Noise Fraction (MNF) transform, to segregate noise in the data (ENVI, 2000). PPI was computed by repeatedly projecting n-D scatter plots on a random unit vector. The extreme pixels in each projection were recorded and the total number of times each pixel was marked as extreme was recorded. A PPI value was set equal to the number of times a pixel was recorded as extreme. Pixels characterized as pure using the PPI were then classified in four classes (one for each urban component) using k-means algorithm. Scatter plots of classified pure pixels were produced and examined to define a set of possible endmembers.

Pixels regarded as possible endmembers were then visually inspected using the higher resolution Ikonos orthophotomap as reference. One endmember was assigned to each urban component using the following criteria: a pixel should successfully represent an urban land cover component and it should have a PPI value higher than a threshold. Since PPI estimation is an iterative process, a threshold value can be reached when the number of pure pixels does not change with further iterations.

3.4. Emissivity estimation

The fraction images derived using LSMA were combined with representative emissivity values for the urban land cover components derived from spectral libraries, to estimate urban surface emissivity. Specifically, a unique emissivity value ε for each pixel was obtained using:

$$\varepsilon = \sum_{k=1}^{n} \varepsilon_k \cdot f_k \tag{5}$$

where ε_k is the emissivity corresponding to endmember k and f_k is the fraction of endmember k within the pixel.

Information included in the ASTER Spectral Library version 2.0 (Baldridge et al., 2009) was utilized to derive representative emissivity values for each component. The ASTER Spectral Library includes spectra of both natural and man-made materials. Specifically it includes spectra of 4 types of vegetation, 52 types of terrestrial soils and 56 types of man-made materials. Moreover it provides the spectral distribution of reflectance ρ, covering all ASTER spectral bands. Assuming Lambertial conditions in the thermal infrared area, emissivity ε_i can be computed using $\varepsilon_i = 1 - \rho_i$, where i is the spectral channel. The ASTER spectral response function (ERSDAC, 2005) was used to adjust the spectral library reflectance values. From the five ASTER TIR bands, LST retrievals are more accurate in the typical spectral region 10–12 μm, where atmospheric transmission is higher and emissivity variations are lower compared to other atmospheric windows, such as the 8–9 μm spectral window (Jiménez-Muñoz and Sobrino, 2010). For this reason, emissivity was derived for the spectral window 10.25–10.95 μm (ASTER band 13), although it could be applied to any ASTER TIR band.

Four types of vegetation are included in the ASTER Spectral Library: dry and green grass, conifer and deciduous trees. The mean value of green grass and conifer trees was considered representative of the vegetation component, according to its definition in this study. Consequently, an emissivity value of 0.987 (in the spectral window 10.25–10.95 μm) was assigned to the vegetation component. For soil, as well as man-made materials types, a global emissivity value could not be assigned. The emissivity values assigned to these components were site-specific and depended on the soil types found in the area and the man-made materials used for construction. Fig. 2 shows emissivity density functions in the spectral window 10.25–10.95 μm (ASTER band 13) of (a) soil and (b) man-made material types found in the ASTER Spectral Library. Emissivity values for different soil types do not display substantial variation; however, this is not the case for man-made material types. The ASTER Spectral Library includes some samples of man-made material types with very low emissivity values, such as aluminum, galvanized steel and copper metals or metallic paint. By selecting the types found in the study area, a representative emissivity value was assigned to each component.

3.5. Accuracy assessment — comparison with ASTER high level products

Assessing the accuracy of SMA derived fractions was outside the scope of this paper. Since the CLAV algorithm was employed to solve LSMA for the first time to the best of our knowledge, the correspondence between coefficients derived from the two approaches was examined. The accuracy of the proposed method was assessed by comparing the estimated emissivity maps (using both CLS and CLAV) to the ASTER emissivity high level product (AST05) provided by the TES algorithm (Gillespie et al., 1998). The latter was considered as the reference dataset. Additionally, the estimated emissivity maps were compared to an emissivity map produced using the NDVI-based algorithm (Jiménez-Muñoz et al., 2006). Since the spatial resolution of the ASTER high level products' is 90 m × 90 m, estimated maps using the proposed method were spatially averaged from 15 m × 15 m to 90 m × 90 m. The size of the sample used for accuracy assessment was approximately 40,000.

Error distributions were examined and several measures were computed to evaluate the accuracy of the estimations (Hyndman & Koehler, 2006). The Mean Square Error (MSE), Root Mean Square

Please cite this article as: Mitraka, Z., et al., Improving the estimation of urban surface emissivity based on sub-pixel classification of high resolution satellite imagery, *Remote Sensing of Environment* (2011), doi:10.1016/j.rse.2011.06.025

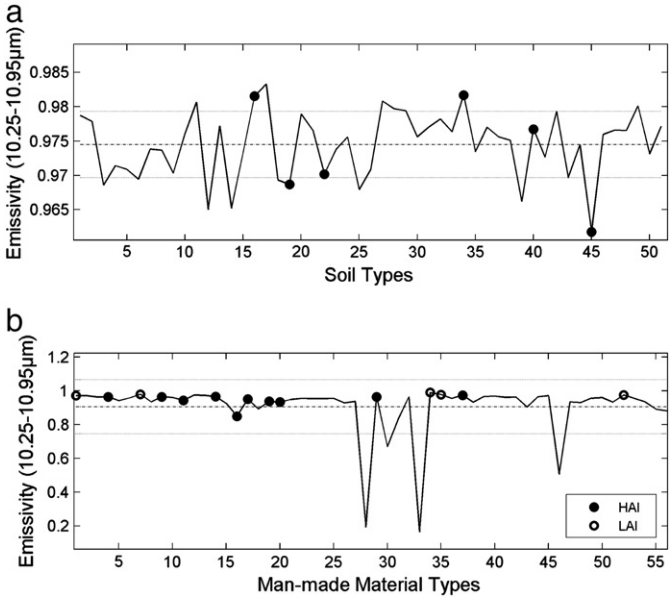

Fig. 2. Emissivities in 10.25–10.95 μm spectral window (ASTER band 13) of a) soil and b) man-made materials types included in the ASTER Spectral Library. The dotted and straight lines represent the mean value and the standard deviation of all samples respectively. Encircled values correspond to those that were selected as representative for the study area ('●' used for the high-albedo and 'O' for low-albedo material types).

Error (RMSE), Bias, Mean Absolute Error (MAE), Median Absolute Error (MdAE), Mean Absolute Percentage Error (MPE), as well as Median Absolute Percentage Error (MdPE) were calculated for all cases:

$$\begin{aligned} MSE &= mean\left((S_i - R_i)^2\right) \\ RMSE &= \sqrt{MSE} \\ Bias &= mean(S_i - R_i) \\ MAE &= mean(|S_i - R_i|) \\ MdAE &= median(|S_i - R_i|) \\ MAPE &= mean(|S_i - R_i| / R_i) \\ MdAPE &= median(|S_i - R_i| / R_i) \end{aligned} \quad (6)$$

where S_i are the estimated and R_i the reference values ($i = 1,\ldots,n$ the number of observations). It is worth noting that accuracy measures based on the median (instead of the mean) are more suitable when the distribution of errors is non-symmetric (Hyndman & Koehler, 2006). On the other hand percentage errors have the advantage of being scale independent so they can be used to evaluate performance across different datasets.

A hypothesis test was performed to examine whether CLAV and CLS derived emissivity maps follow the same distribution. Specifically, the (nonparametric) Wilcoxon rank-sum test was applied to assess whether the two samples of observations have equally large values. The Wilcoxon test requires independent observations and since estimated emissivity values are not independent due to spatial autocorrelation, subsamples were selected in which a distance of 25 pixels was imposed in consecutively sampled pixels. The test was performed in the selected subsamples which were considered free from spatial autocorrelation.

In addition, LST maps were produced using the above mentioned emissivity maps in order to examine the impact of estimated

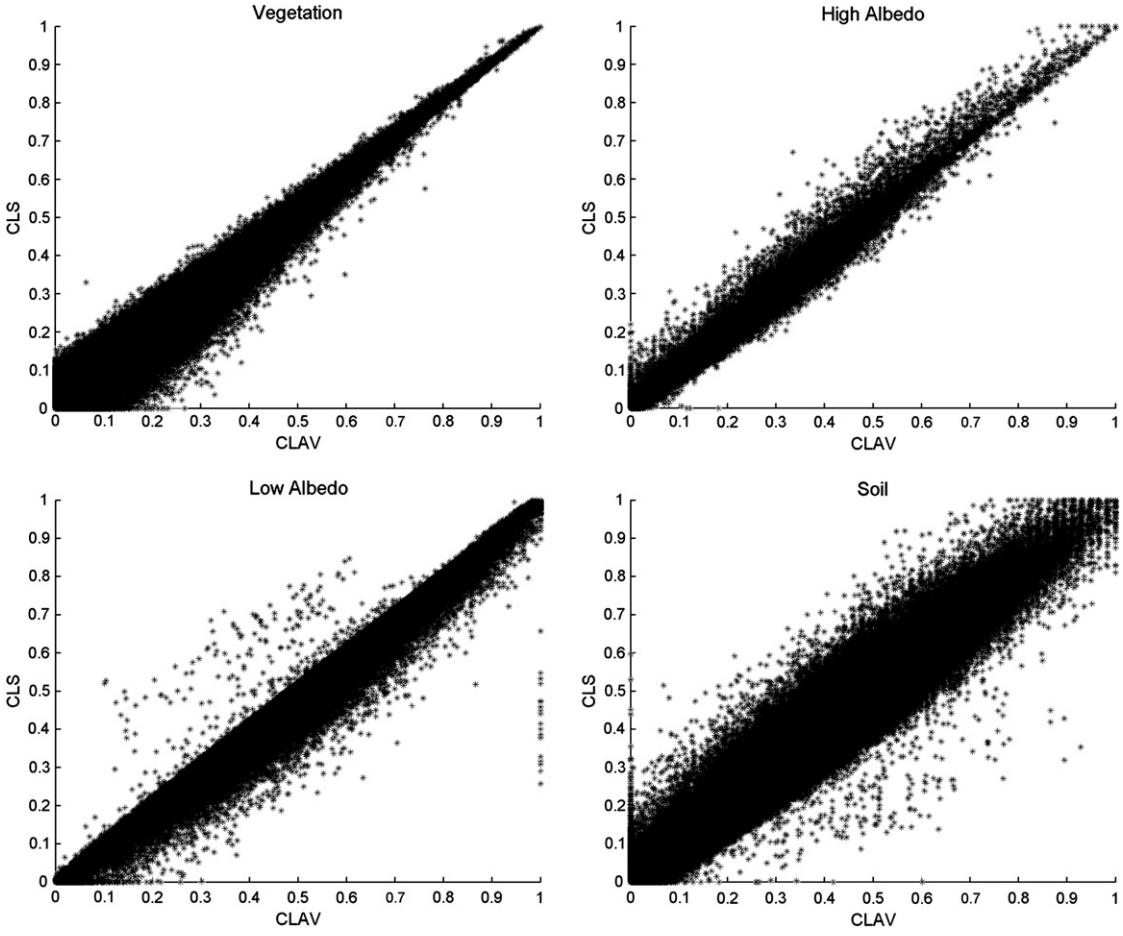

Fig. 3. Scatter-plots of the associations between CLS and CLAV derived coefficients: a) vegetation, b) high-albedo c) low-albedo d) soil.

Please cite this article as: Mitraka, Z., et al., Improving the estimation of urban surface emissivity based on sub-pixel classification of high resolution satellite imagery, *Remote Sensing of Environment* (2011), doi:10.1016/j.rse.2011.06.025

emissivity in LST derivation. LST maps were derived using the approach of Jiménez-Muñoz and Sobrino (2003), adapted to the ASTER channel 13 (Jiménez-Muñoz & Sobrino, 2010). The MODIS Precipitable Water product (LAADS, 2010) corresponding to the respective scene was used in LST estimation to account for the atmospheric effect. The derived LST maps were also compared to the ASTER LST high level product (AST08). Error distributions of estimated vs. reference LSTs were also examined and error measurements (Eq. (6)) were computed for all cases.

4. Results and discussion

4.1. Spectral mixture analysis

The first step for spectral unmixing is the selection of endmembers. After resampling the SWIR (5–9) bands to match the spatial resolution of the VNIR (1–4) bands (pixel size 15 m × 15 m), the PPI was applied and 3.52% of the total number of pixels was recognized as pure. Pure pixels were then classified into four classes, one for every urban land cover component; vegetation, high-albedo, low-albedo and soil classes corresponded in 19,194, 5784, 12,870 and 18,607 pixels respectively. Scatter-plots of the classified pure pixels were examined and possible endmembers were identified as being extremes in the scatter-plots. Since PPI estimation is an iterative process, a threshold value is reached when the number of pure pixel does not change with further iterations. The threshold PPI value in this study was found equal to 1500. Pixels having a PPI value below that threshold could not be selected as endmembers. After visual inspection of the pixels regarded as possible endmembers, one pixel was finally assigned to each of the four land cover components and was used as an endmember for spectral unmixing.

The fractional covers of urban components in Eqs. (3), (4) were estimated by CLS and CLAV. Fig. 3 depicts scatter-plots of the associations between CLS and CLAV derived coefficients. One may clearly observe a heteroskedastic relationship for coefficients that correspond to vegetation with decreasing levels of variance as their magnitude approaches unity. Essentially as the proportion of vegetation in a pixel increases, the CLAV coefficients tend to approximate the ones derived from CLS. This phenomenon is not observed in the three remaining land cover types. It is worth noticing that the association appears less strong for the soil land cover component compared to the ones observed for HAI and LAI land cover components.

Fig. 4 shows the fraction images — vegetation, high-albedo, low-albedo and soil — derived using CLAV coefficients. Pixel values of a fraction image represent the areal proportions of each endmember within a pixel. The area that corresponds to sea always appears black as sea water was excluded from all computations.

In the vegetation fraction image, agricultural areas appear to be brighter. In fact, Heraklion is a city with very little urban vegetation and this is clearly depicted in the vegetation fraction image. In the high-albedo fraction image, commercial, industrial and residential areas as well as quarries are included. The low-albedo endmember captured surfaces that appear as dark in visible, like roads, wet soils and, in some cases, shadows. Although it is difficult to find areas of the size of the pixel containing pure bare soil in the broader area of Heraklion, the soil fraction image reveals presence of the soil component in many pixels of the image. The lower values in soil fraction images appear in the city of Heraklion, which is in accord to prior expectations.

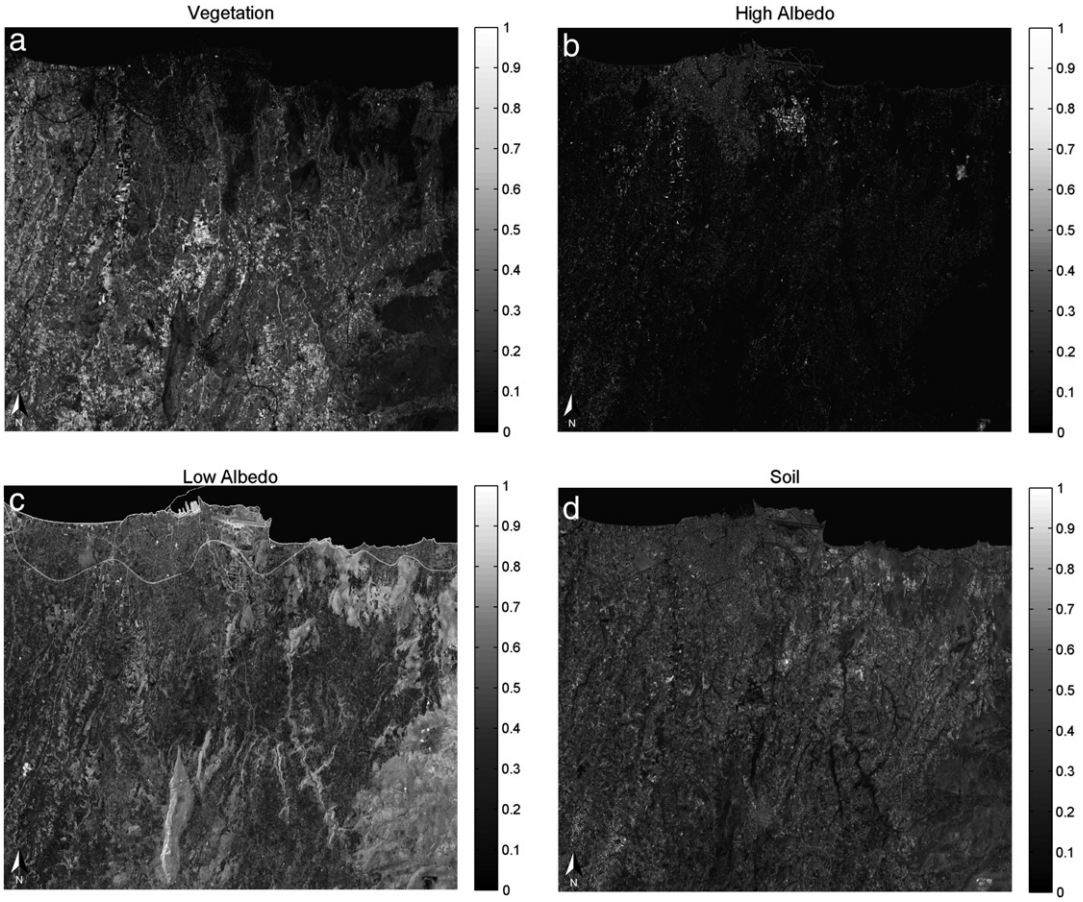

Fig. 4. The land cover fractions estimated using Spectral Mixture Analysis via CLAV: a) vegetation, b) high-albedo c) low-albedo d) soil. White color corresponds to 1, black to 0 and the gray variations represent the intervals 0–1. Since sea water is masked out of any computation, it appears black.

Please cite this article as: Mitraka, Z., et al., Improving the estimation of urban surface emissivity based on sub-pixel classification of high resolution satellite imagery, *Remote Sensing of Environment* (2011), doi:10.1016/j.rse.2011.06.025

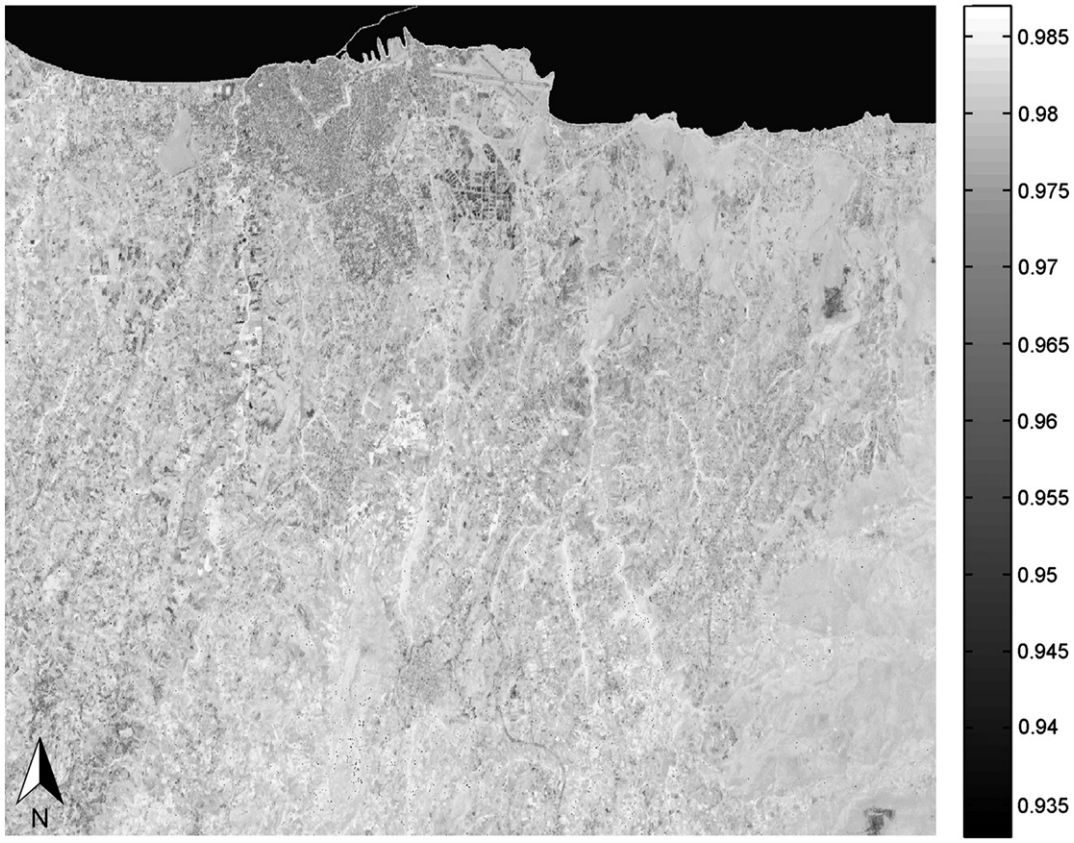

Fig. 5. Map of estimated emissivity values in the 10.25–10.95 μm spectral window (ASTER band 13) produced for the study area using the proposed methodology implemented via CLAV.

4.2. Emissivity maps

To estimate emissivity following the proposed method, representative emissivity values are required for the four urban land cover components. In the case of vegetation, the global emissivity value of 0.987 in the 10.25–10.95 μm spectral window (ASTER band 13) was used. For soil, as well as man-made materials types, the representative emissivity values are site-specific. Seven soil types were selected from the ASTER Spectral Library and were considered representative for the soil component of the study area: light yellowish brown clay (aridisol), brown to dark brown sand (entisol), gray/dark brown extremely stoney coarse sandy (inceptisol), gray silty clay (mollisol), brown to dark brown clay (vertisol) and alluvial sand (entisol). These soil types have a mean emissivity value of 0.973 in the 10.25–10.95 μm spectral window (ASTER band 13) which was used as representative for the soil component.

Likewise, ten bright construction materials that are present in the study area were selected for the high-albedo component: one type of construction tar and two of construction concrete, red smooth-faced brick, plate window glass, white marble, olive green gloss paint, black gloss paint, steel metal, and white coating. The mean emissivity value (equal to 0.944) of those man-made material types in the 10.25–10.95 μm spectral window (ASTER band 13) was used as representative for the high-albedo component.

Five dark man-made materials were selected as representative for the low-albedo component: one type of construction asphalt, one type of construction concrete, two types of dark roofing materials (copper metal and black tar paper) and one general construction material (black paint). The mean emissivity value of these material types in the 10.25–10.95 μm spectral window (ASTER band 13) is 0.979. Interpreting the low-albedo fraction image, it is obvious that a low-albedo component is present in most of the study area. As explained earlier, this happens because the low-albedo fraction contains crops with water, wet soil and shaded areas. The mean emissivity of water types found in ASTER Spectral Library is 0.990. The mean value of dark man-made material types and water, equal to 0.9845, was considered representative and assigned to the low-albedo component.

The emissivity map in the 10.25–10.95 μm spectral window (ASTER band 13), was derived by using the cover fractions estimated by CLAV and the representative emissivity values and is shown in Fig. 5. Sea water is masked out of any computations and the respective area appears in the figure as black. The topography of the area is clearly outlined in the derived emissivity map. Low emissivity values appear in the commercial and residential area, whereas even lower values are estimated for the industrial area in the eastern part of the city. The two quarries that are included in the study area also appear with low emissivity values. It is remarkable that, the green areas around the city's ancient walls, where the majority of the parks are located, appear to have high emissivity values. In addition, crops and areas with trees appear also with high emissivity values.

Table 1 presents measures of accuracy computed for estimated emissivity using both CLAV and CLS vs. the ASTER emissivity high level

Table 1
Error measurements for emissivity differences between estimated and reference values from ASTER emissivity high level product and from NDVI-based emissivity (Jiménez-Muñoz et al., 2006).

	Estimated emissivity vs. ASTER product		NDVI-based emissivity vs. ASTER product
	CLAV	CLS	
MSE	0.000218	0.000222	0.000441
RMSE	0.014777	0.014912	0.021005
Bias	−0.012392	−0.012725	−0.018831
MAE	0.013302	0.013693	0.019367
MdAE	0.014600	0.014550	0.021657
MPE	0.013367	0.013760	0.019451
MdPE	0.014688	0.014633	0.021765

Please cite this article as: Mitraka, Z., et al., Improving the estimation of urban surface emissivity based on sub-pixel classification of high resolution satellite imagery, *Remote Sensing of Environment* (2011), doi:10.1016/j.rse.2011.06.025

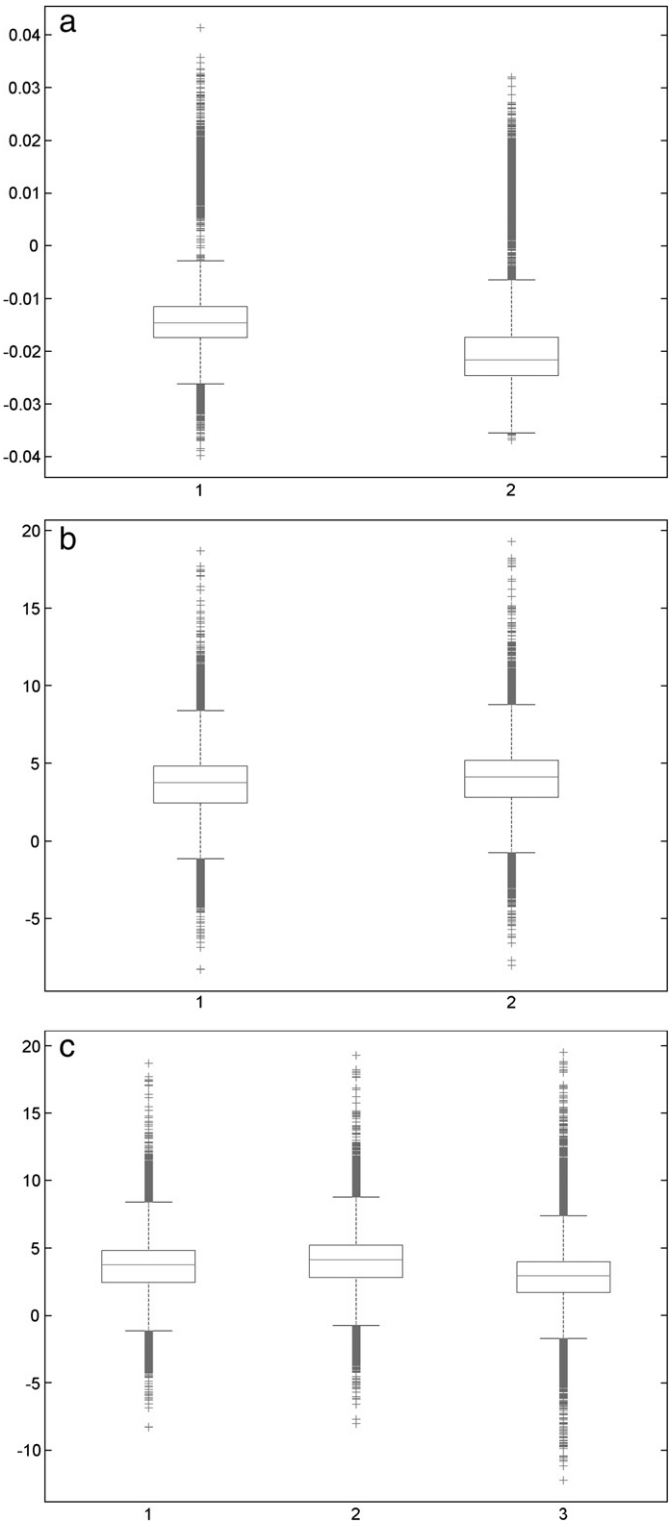

Fig. 6. Box-plots of error distributions. Box-plots are graphical representations of population distributions. The line in the center of the box refers to the mean value of the population, while inside the box lie the 50% of the observations. The tips outside the box include the rest of the observations and whatever lies outside the box tips is considered an outlier. a) Estimated emissivity (1) and NDVI-based emissivity (2) vs. reference AST05 emissivity product, b) estimated LST (1) and NDVI-based LST (2) estimated using Jiménez-Muñoz and Sobrino (2010) vs. LST calculated using AST05 emissivity product and c) estimated LST (1), NDVI-based LST (2) and LST calculated using AST05 emissivity product (3) vs. AST08 LST product.

product. The same measures computed for NDVI-based emissivity (Jiménez-Muñoz et al., 2006) are also presented in Table 1 for comparison. It can be observed that CLAV slightly outperforms CLS according to all measures. These differences although small, are statistically significant as the magnitude of the p-value (2.526e-05) of the Wilcoxon test provided very strong evidence against the null hypothesis which states that the emissivity distributions are equivalent. An RMSE of 0.14777 was observed in estimated emissivity using CLAV, while the respective value for NDVI-based emissivity is 0.21005. It should be noted that all error measurements computations were performed in 90 m × 90 m spatial resolution and the sample size was approximately 40,000 in all cases. The error distributions of estimated against reference emissivity values are shown in Fig. 6a) in the form of box-plot. The error distribution of estimated emissivity is shown in the first box-plot of Fig. 6a), while the error distribution of NDVI-based emissivity is shown in the second box-plot of Fig. 6a). Both the proposed method and the NDVI-based method systematically underestimate emissivity compared to the ASTER product. 50% of the estimated emissivity error distribution lies between −0.017421 and −0.011543, while the respective values for the NDVI-based emissivity error distribution are −0.024644 and −0.017372.

Table 2
Error measurements for LST differences between estimated and reference LST values derived using the algorithm proposed by Jiménez-Muñoz and Sobrino (2010) and ASTER emissivity high level product (AST05). Error measurements for LST derived using NDVI-based emissivity vs. LST derived using ASTER emissivity high level product are also presented.

	Estimated LST vs. LST using ASTER emissivity product		LST using NDVI-based emissivity vs. LST using ASTER emissivity product
	CLAV	CLS	
MSE	0.667383	0.678905	1.358568
RMSE	0.816935	0.823957	1.165576
Bias	0.678260	0.695849	1.039006
MAE	0.731220	0.752199	1.070245
MdAE	0.800052	0.796981	1.193036
MPE	0.002333	0.002400	0.003416
MdPE	0.002555	0.002545	0.003813

Tables 2 and 3 present the error measurements for the estimated LST vs. LST estimated using the ASTER emissivity high level product and ASTER LST high level product respectively. Again, all error measurements for LST derived using the NDVI-based emissivity are presented for comparison. The Jiménez-Muñoz and Sobrino (2010) LST retrieval scheme was used to estimate LST using estimated emissivity, ASTER emissivity product and NDVI-based emissivity. A general observation regarding the error measurements of Tables 2 and 3 illustrates the relatively high values in Table 3 compared to those observed in Table 2; this difference is probably due to the LST estimation algorithm. The relatively low MAPE and MdAPE values justify this claim. RMSE values presented in Tables 2 and 3 indicated an improvement in LST estimation of about 0.35 K with the use of the emissivity derived using the proposed method compared to LST

Table 3
Error measurements for LST differences between estimated LST and ASTER LST high level product (AST08). Error measurements for LST derived using NDVI-based emissivity vs. ASTER LST high level product are also presented.

	Estimated LST vs. ASTER LST product		LST using NDVI-based emissivity vs. ASTER LST product
	CLAV	CLS	
MSE	15.743191	16.337294	19.182518
RMSE	3.967769	4.041941	4.379785
Bias	3.379034	3.516132	3.859289
MAE	3.403850	3.544151	3.879267
MdAE	3.655813	3.732345	4.114125
MPE	0.010983	0.011438	0.012518
MdPE	0.011794	0.012042	0.013278

Please cite this article as: Mitraka, Z., et al., Improving the estimation of urban surface emissivity based on sub-pixel classification of high resolution satellite imagery, *Remote Sensing of Environment* (2011), doi:10.1016/j.rse.2011.06.025

derived using NDVI-based emissivity. Although CLAV does not dramatically outperform CLS in Tables 2 and 3, one may observe again that it performs better according to all examined criteria.

The first box-plot of Fig. 6b) depicts the error distribution of estimated LST against LST derived using the ASTER emissivity product. The error distribution of LST derived using NDVI-based emissivity against LST derived using the ASTER emissivity product is shown in the second box-plot of Fig. 6b). It can be observed that 50% of estimated LST error distribution lies between 0.619046 and 0.963039, while the respective values of the error distribution of LST derived using NDVI-based emissivity are 0.934235 and 1.372766. The above observation along with the error measurements of Table 2 indicate that the estimated emissivity contributes to improvement in LST estimation compared to the NDVI-base emissivity, although more evidence is required to justify this claim.

Fig. 6c) shows the error distributions of estimated LST (first box-plot) and NDVI-based LST (second box-plot) against the ASTER LST high level product. As noted earlier from Table 3, derived LSTs present a deviation from ASTER LST product. To test if this is due to the LST retrieval scheme that is used (Jiménez-Muñoz & Sobrino, 2010) the LST derived using this scheme and ASTER emissivity product was compared to the ASTER LST product. The third box-plot of Fig. 6c) shows the error distribution of LST derived using ASTER emissivity product against the ASTER LST product (RMSE = 3.3799). 50% of estimated LST error lies in [2.438046, 4.823311] while the respective interval for NDVI-based LST is [2.815277, 5.201280]. This along with previous remarks is an indication that the proposed method of emissivity estimation may improve LST estimation.

5. Conclusions

In this paper, a new methodology for deriving land surface emissivity over urban areas is presented. Surface emissivity over urban areas is essential for surface temperature estimation that is related to energy budget and is significant to a range of earth science related applications along with relevant planning and management practices.

The proposed methodology is based on spectral mixture analysis. The urban surface is assumed to be consisted of three fundamental land cover components, namely vegetation, impervious and soil. Due to the complexity of the urban environment, the impervious component is further divided into two impervious land cover components. The main advantage of the proposed approach is mixed pixel handling, which is essential when using satellite images of this spatial resolution to capture biophysical parameters in urban environment. Therefore, the emissivity dependence on surface type and its physical conditions are taken into account in sub-pixel level. Furthermore, the angular variation of emissivity is indirectly taken into account, since the fraction of each component depends on the observation angle. The method proposed here can be used for time series derivation since it is image-based. Moreover unlike other emissivity estimation methods that require atmospherically corrected data, the proposed method can be directly applied, with no need of atmospheric correction. The methodology is applicable to visible and near infrared satellite imagery and enables direct derivation of emissivity maps from most multispectral satellite sensors, which is considered an advantage over the TES method. Furthermore, modeling the urban surface using the proposed method enables consideration of fractional cover of impervious surfaces, in contrast to the NDVI method. Finally, implementation of SMA via a CLAV algorithm is considered an advantage over the widely used CLS method, as the former has been shown to be particularly effective when the distribution of the response variable is prone to outliers.

The results of the proposed method may be improved if advanced SMA techniques are used for the derivation of fractional covers like Multiple Endmember Spectral Mixture Analysis, or Neural Networks. In addition, a combination of image and reference endmembers may result in more accurate correspondence between urban land cover components and reference emissivity values.

Acknowledgment

The research leading to these results has received funding from the European Community's Seventh Framework Programme (FP7/2007–2013) under grant agreement no 211345 (BRIDGE Project).

References

Adams, J., Sabol, D., Kapos, V., Filho, R., Roberts, D., Smith, M., et al. (1995). Classification of multispectral images based on fractions of endmembers: Application to land-cover change in the Brazilian Amazon. *Remote Sensing of Environment*, *52*, 137–154.

Arnfield, J. A. (2003). Two decades of urban climate research: A review of turbulence, exchanges of energy and water, and the urban heat island. *International Journal of Climatology*, *23*, 1–26.

Baldridge, A. M., Hook, S. J., Grove, C. I., & Rivera, G. (2009). The ASTER Spectral Library Version 2.0. *Remote Sensing of Environment*, *113*, 711–715.

Becker, F., & Li, Z. L. (1990). Toward a local split window method over land surface. *International Journal of Remote Sensing*, *11*, 369–393.

Becker, F., & Li, Z. L. (1995). Surface temperature and emissivity at various scales: Definition, measurement and related problems. *Remote Sensing Reviews*, *12*, 225–253.

Boardman, J. W., Kruse, F. A., & Green, R. O. (1995). Mapping target signatures via partial unmixing of AVIRIS data. *Summaries of the Fifth Annual JPL Airborne Geoscience Workshop* (pp. 23–26). Pasadena, CA: Jet Propulsion Laboratory Publications.

Chrysoulakis, N. (2003). Estimation of the all-wave urban surface radiation balance by use of ASTER multispectral imagery and in situ spatial data. *Journal of Geophysical Research*, *108*(D18), 4582, doi:10.1029/2003JD003396.

Chrysoulakis, N., Abrams, M., Feidas, H., & Arai, K. (2010). Comparison of atmospheric correction methods using aster data for the area of Crete: The ATMOSAT project. *International Journal of Remote Sensing*, *31*, 6347–6385.

Chrysoulakis, N., Vogt, R., Young, D., Grimmond, C. S. B., Spano, D., & Marras, S. (2009). ICT for urban metabolism: The case of BRIDGE. In V. Wohlgemuth, B. Page, & K. Voigt (Eds.), *Proceedings of EnviroInfo2009: Environmental informatics and industrial environmental protection: Concepts, methods and tools. Hochschule für Technik und Wirtschaft, Vol. 2*. (pp. 183–193).

Clapham, W. B., Jr. (2003). Continuum-based classification of remotely sensed imagery to describe urban sprawl on a watershed scale. *Remote Sensing of Environment*, *86*, 322–340.

Coll, C., Caselles, V., Sobrino, J. A., & Valor, E. (1994). On the atmospheric dependence of the split-window equation for land surface temperature. *International Journal of Remote Sensing*, *15*, 105–122.

Dash, P., Gottsche, F. M., Olesen, F. S., & Fischer, H. (2002). Land surface temperature and emissivity estimation from passive sensor data: theory and practice — Current trends. *International Journal of Remote Sensing*, *23*, 2563–2594.

Dielman, T. E. (2005). Least absolute value regression: Recent contributions. *Journal of Statistical Computation and Simulation*, *75*, 263–286.

Dielman, T. E. (2009). Least absolute value vs. least squares estimation and inference procedures in regression models with asymmetric error distributions. *Journal of Modern Statistical Methods*, *8*, 147–160.

ENVI (2000). *ENVI user's guide*. Boulder, Colorado. CA: Research Systems Inc.

ERSDAC (2005). *ASTER user's guide. Part I general (ver. 4)*. : Earth Remote Sensing Data Analysis Center.

Gill, P. E., Murray, W., & Wright, M. H. (1981). *Practical optimization*. London, UK: Academic Press.

Gillespie, A., Rokugawa, S., Matsunaga, T., Cothern, J. S., Hook, S., & Kahle, A. B. (1998). A temperature and emissivity separation algorithm for advanced spaceborne thermal emission and reflection radiometer (ASTER) images. *IEEE Transactions on Geoscience and Remote Sensing*, *36*, 1113–1126.

Hyndman, R. J., & Koehler, A. B. (2006). Another look at measures of forecast accuracy. *International Journal of Forecasting*, *22*, 679–688.

Jensen, J. R. (1983). Biophysical remote sensing. *Annals of the Association of American Geographers*, *73*, 111–132.

Ji, M., & Jensen, J. R. (1999). Effectiveness of subpixel analysis in detecting and quantifying urban imperviousness from Landsat Thematic Mapper Imagery. *Geocarto International*, *14*, 31–39.

Jiménez-Muñoz, J. C., & Sobrino, J. A. (2003). A generalized single channel method for retrieving land surface temperature from remote sensing data. *Journal of Geophysical Research*, *108*, doi:10.1029/2003JD003480.

Jiménez-Muñoz, J. C., & Sobrino, J. A. (2010). A single-channel algorithm for land-surface temperature retrieval from ASTER data. *IEEE Geoscience and Remote Sensing Letters*, *7*, 1.

Jiménez-Muñoz, J. C., Sobrino, J. A., Gillespie, A., Sabol, D., & Gustafson, W. T. (2006). Improved land surface emissivities over agricultural areas using ASTER NDVI. *Remote Sensing of Environment*, *103*, 474–487.

Kealy, P. S., & Gabell, A. R. (1990). Estimation of emissivity and temperature using alpha coefficients. *Proceedings of second T IMS workshop* (pp. 90–95). Pasadena, CA: (Jet Propulsion Laboratory), JPL Pub.

Kennedy, C., Pincetl, S., & Bunje, P. (2011). The study of urban metabolism and its applications to urban planning and design. *Environmental Pollution*, *159*, 1965–1973.

Koenker, R. (2011). *R package 'quantreg' version 4.57*.

LAADS (2010). *The level 1 and atmosphere archive and distribution system.* Goddard Distributed Active Archive Center http://ladsweb.nascom.nasa.gov/data

Lambin, E. F., Turner, B. L., Geist, H. J., Agbola, S. B., Angelsen, A., Bruce, J. W., et al. (2001). The causes of land-use and land-cover change: Moving beyond the myths. *Global Environmental Change*, *11*, 261–269.

Lipakis, M., Chrysoulakis, N., & Kamarianakis, Y. (2008). Shoreline extraction using satellite imagery. In E. Pranzini, & E. Wetzel (Eds.), *Beach erosion monitoring. Results from BEACHMED/e-OpTIMAL project (Optimization des Techniques Integrées de Monitorage Appliquées aux Lottoraux) INTERREG IIIC South* (pp. 81–95). Florence, Italy: Nuova Grafica Fiorentina.

LPDAAC (2010). *ASTER land products.* : Land Processes Distributed Active Archive Center http://edcdaac.usgs.gov/aster/asterdataprod.asp

Lu, D., & Weng, Q. (2004). Spectral mixture analysis of the urban landscape in Indianapolis with Landsat ETM+ imagery. *Photogrammetric Engineering and Remote Sensing*, *70*, 1053–1062.

Lu, D., & Weng, Q. (2006). Use of impervious surface in urban land use classification. *Remote Sensing of Environment*, *102*, 146–160.

Powell, R. L., Roberts, D. A., Dennison, P. E., & Hess, L. L. (2007). Sub-pixel mapping of urban land cover using multiple endmember spectral mixture analysis: Manaus, Brazil. *Remote Sensing of Environment*, *106*, 253–267.

Prata, A. J. (1993). Land surface temperature derived from the advanced very high resolution radiometer and the along-track scanning radiometer. 1. Theory. *Journal of Geophysical Research*, *98*, 16689–16702.

Prata, A. J. (1994). Land surface temperature derived from the advanced very high resolution radiometer and the along-track scanning radiometer. 2. Experimental results and validation of AVHRR algorithms. *Journal of Geophysical Research*, *99*, 13025–13058.

Prata, A. J. (2002). *Land surface temperature measurement from space: AATSR algorithm theoretical basis document.* Australia: CSIRO Atmospheric Research Aspendale.

Ramsey, M. S., & Christensen, P. R. (1998). Mineral abundance determination: Quantitative deconvolution of thermal emission spectra. *Journal of Geophysical Research*, *103*, 577–596.

Rashed, T., Weeks, J. R., Stow, D., & Fugate, D. (2005). Measuring temporal compositions of urban morphology through spectral mixture analysis: Towards a soft approach to change analysis in crowded cities. *International Journal of Remote Sensing*, *26*, 699–718.

Ridd, M. K. (1995). Exploring a V-I-S (vegetation-impervious surface-soil) model for urban ecosystem analysis through remote sensing: Comparative anatomy for cities. *International Journal of Remote Sensing*, *16*, 2165–2185.

Roberts, D. A., Smith, M. O., & Adams, J. B. (1993). Green vegetation, non-photosynthetic vegetation, and soils in AVIRIS data. *Remote Sensing of Environment*, *44*, 255–269.

Salisbury, W., & D'Aria, D. M. (1992). Emissivity of terrestrial materials in the 8–14 mm atmospheric window. *Remote Sensing of Environment*, *42*, 83–106.

Salisbury, J. W., & D'Aria, D. M. (1994). Emissivity of terrestrial materials in the 3–5 μm atmospheric window. *Remote Sensing of Environment*, *47*, 345–361.

Salisbury, J. W., D'Aria, D. M., & Wald, A. (1994). Measurements of thermal infrared spectral reflectance of frost, snow, and ice. *Journal of Geophysics Research*, *99*, 24,235–24,240.

Smith, M. O., Ustin, S. L., Adams, J. B., & Gillespie, A. R. (1990). Vegetation in deserts: I. A regional measure of abundance from multispectral images. *Remote Sensing of Environment*, *31*, 1–26.

Snyder, W. C., & Wan, Z. (1998). BRDF models to predict spectral reflectance and emissivity in the thermal infrared. *IEEE Transactions on Geoscience and Remote Sensing*, *36*, 214–225.

Snyder, W. C., Wan, Z., Zhang, Y., & Feng, Y. (1997). Thermal infrared (3 ± 14 μm) bidirectional reflectance measurements of sands and soils. *Remote Sensing of Environment*, *60*, 101–109.

Snyder, W. C., Wan, Z., Zhang, Y., & Feng, Y. -Z. (1998). Classification-based emissivity for land surface temperature measurement from space. *International Journal of Remote Sensing*, *19*, 2753–2774.

Sobrino, J. A., Caselles, V., & Becker, F. (1990). Significance of the remotely sensed thermal infrared measurements obtained over a citrus orchard. *ISPRS Photogrammetric Engineering and Remote Sensing*, *44*, 343–354.

Sobrino, J. A., & Cuenca, J. (1999). Angular variation of thermal infrared emissivity for some natural surfaces from experimental measurements. *Applied Optic*, *38*, 3931–3936.

Sobrino, J. A., Li, Z. L., Stoll, M. P., & Becker, F. (1996). Multi-channel and multi-angle algorithms for estimating sea and land surface temperature with ATSR data. *International Journal of Remote Sensing*, *17*(11), 2089–2114.

Sobrino, J. A., & Raissouni, N. (2000). Toward remote sensing methods for land cover dynamic monitoring. Application to Morocco. *International Journal of Remote Sensing*, *21*, 353–366.

Song, C., Woodcock, C. E., Seto, K. C., Lenny, M. P., & Macomber, S. A. (2001). Classification and change detection using Landsat TM data, when and how to correct atmospheric effects? *Remote Sensing of Environment*, *75*, 230–244.

Tonooka, H., Sakuma, F., Kudoh, M., & Iwafune, K. (2003). ASTER/TIR onboard calibration status and user-based recalibration. *Proceedings of SPIE*, *5234*, 191–201.

Valor, E., & Casseles, V. (1996). Mapping Land surface emissivity from NDVI: Application to European African and South American areas. *Remote Sensing of Environment*, *57*, 167–184.

Voogt, J. A., & Oke, T. R. (2003). Thermal remote sensing of urban climates. *Remote Sensing of Environment*, *86*, 370–384.

Watson, K. (1992). Spectral ratio method for measuring emissivity. *Remote Sensing of Environment*, *42*, 113–116.

Weng, Q. (2009). Thermal infrared remote sensing for urban climate and environmental studies: Methods, applications, and trends. *ISPRS Journal of Photogrammetry and Remote Sensing*, *64*, 335–344.

Weng, Q., Hu, X., & Liu, H. (2009). Estimating impervious surfaces using linear spectral mixture analysis with multitemporal ASTER images. *International Journal of Remote Sensing*, *30*(18), 4807–4830.

Weng, Q., Lu, D., & Liang, B. (2006). Urban surface biophysical descriptors and land surface temperature variations. *Photogrammetric Engineering and Remote Sensing*, *72*(11), 1275–1286.

Yang, L., Huang, C., Homer, C. G., Wylie, B. K., & Coan, M. J. (2003). An approach for mapping large-scale impervious surfaces: Synergistic use of Landsat-7 ETM+ and high spatial resolution imagery. *Canadian Journal of Remote Sensing*, *29*, 230–240.

Yu, Y., Privette, J. L., & Pinheiro, A. C. (2008). Evaluation of split-window land surface temperature algorithms for generating climate data records. *IEEE Transactions on Geoscience and Remote Sensing*, *46*, 179–192.

Please cite this article as: Mitraka, Z., et al., Improving the estimation of urban surface emissivity based on sub-pixel classification of high resolution satellite imagery, *Remote Sensing of Environment* (2011), doi:10.1016/j.rse.2011.06.025